PERGAMON

International Journal of Heat and Mass Transfer 45 (2002) 2229–2242

International Journal of HEAT and MASS TRANSFER

www.elsevier.com/locate/ijhmt

A three-dimensional model of droplet impact and solidification

M. Pasandideh-Fard, S. Chandra, J. Mostaghimi *

Department of Mechanical and Industrial Engineering, Centre for Advanced Coating Technologies, University of Toronto, 5 King's College Road, Toronto, Ont., Canada M5S 3G8

Received 10 May 2001; received in revised form 20 October 2001

Abstract

A three-dimensional model has been developed to simulate the fluid dynamics, heat transfer and phase-change that occur when a molten metal droplet falls onto a flat substrate. The model is an extension of one developed by Bussmann et al. [Phys. Fluids 11 (1999) 1406] and combines a fixed-grid control volume discretization of the fluid flow and energy equations with a volume-tracking algorithm to track the droplet free surface, and an improved fixed velocity method to track the solidification front. Surface tension is modeled as a volume force acting on fluid near the free surface. Contact angles are applied as a boundary condition at liquid–solid contact lines. The energy equations in both the liquid and solid portions of the droplet are solved using the Enthalpy method. Heat transfer within the substrate is by conduction alone. Thermal contact resistance at the droplet–substrate interface is included in the model. We studied the deposition of tin droplets on a stainless steel surface using both experiments and numerical simulations. The results of two different scenarios are presented: the normal impact of a 2.7 mm tin droplet at 1 m/s, and of the oblique impact of a 2.2 mm tin droplet at 2.35 m/s onto a surface inclined at 45° to the horizontal. Images obtained from numerical model were compared with experimental photographs and found to agree well.

1. Introduction

Traditional manufacturing techniques can be broadly classified into one of two techniques: machining or casting. Machining requires removal of material from a stock piece, resulting in a great deal of wastage. Casting wastes less material, since only the required amount of melt is poured into a mould, but the design and fabrication of moulds is a costly and time-consuming process. Recently developed spray-forming methods offer a fundamentally different means of making complex shaped parts, with little wastage and without having to build moulds. Streams of molten droplets – which may be of metal, wax, plastic, or ceramic – are propelled onto a solid substrate, and by maneuvering both the spray and substrate intricate components can be built up.

Though spray forming is conceptually an extremely elegant technology, in practice it has not proved easy to implement. A number of difficulties have been encountered, including failure of droplets to bond to each other, formation of pores at the interface between droplets, and residual stresses in the finished part. Many of the same problems have also been observed in thermal spray coating processes, in which molten droplets are sprayed onto a solid surface where they freeze and form a protective coating. Achieving good material properties in all spray deposition technologies requires careful control of droplet size, temperature and impact velocity. Since the operational costs of thermal spray equipment is high, it is more economical to optimize operating parameters using computational models rather than experiments.

There exists a considerable literature describing numerical models of droplet impact on a solid surface, which also find application in other industrial processes such as agricultural spraying, ink jet printing, spray painting, spray cooling of hot surfaces, fire fighting, and solder deposition on circuit boards. Computing fluid flow and heat transfer during droplet impact is a complex problem since it involves modeling free surfaces undergoing large deformations and moving

* Corresponding author. Tel.: 1-416-978-5604; fax: 1-416-978-7753.

E-mail address: mostag@mie.utoronto.ca (J. Mostaghimi).

0017-9310/02/$ - see front matter
PII: S0017-9310(01)00336-2

Nomenclature

C	specific heat
D	splat diameter
D_o	diameter of spherical droplet
f	volume of fluid fraction
$\overrightarrow{F_b}$	body force
h	enthalpy
H_f	latent heat of fusion
k	thermal conductivity
$\hat{n}_l$	unit normal to the liquid free surface
$\hat{n}_r$	redirected unit normal to the liquid free surface
$\hat{n}_s$	unit normal to the solidification front
p	pressure
q	heat flux
R_c	thermal contact resistance at droplet/substrate interface
t	time
T	temperature
T_m	droplet melting point
v	volume
$\overrightarrow{V}$	velocity
V_o	droplet impact velocity

Greek symbols

α	angle between $\hat{n}_l$ and $\hat{n}_s$
β	$= k/C$
Θ	liquid–solid volume fraction
θ_{ls}	liquid–solid contact angle
υ	kinematic viscosity
ξ	spread factor
ρ	density
ϕ	source term in energy equation $(= H_f k_l/C_l)$

Subscripts

l	liquid
s	solid
w	substrate

Dimensionless numbers

Ec	Eckert number $(V_o^2/(C_l \Delta T))$
Re	Reynolds number $(V_o D_o/\upsilon)$

liquid–solid–gas contact lines. Heat transfer calculations must include convection in the liquid and conduction in the solid, while accounting for steep temperature gradients in a rapidly deforming liquid layer, coupled with conduction in the substrate.

Harlow and Shannon [2] were the first to simulate droplet impact on a solid surface. They used a "marker-and-cell" (MAC) finite-difference method to solve the fluid mass and momentum conservation equations, while neglecting the effect of viscosity and surface tension to simplify the problem. Tsurutani et al. [3] enhanced the MAC model to include surface tension and viscosity effects, and also considered heat transfer from a hot surface to a cold liquid drop as it spread on the surface. Trapaga and Szekely [4] applied a commercial code, FLOW-3D [5], that uses the "volume of fluid" (VOF) method, to study impact of molten particles in a thermal spray process. Liu et al. [6] employed another VOF based code, RIPPLE [7,8], to simulate molten metal droplet impact. Pasandideh-Fard et al. [9] applied a modified SOLA-VOF [10] method to model the impact of water droplets in which varying amounts of a surfactant were dissolved to modify the liquid–solid contact angle. They extended the model [11] to include heat transfer and phase change, and simulated freezing of molten tin droplets falling on a stainless steel plate. Zhao et al. [12] formulated a finite-element model of droplets deposited on solid surfaces. Adaptive-grid finite element methods were used first by Fukai et al. [13] to simulate water droplet impact, and later by Bertagnolli et al. [14] and Waldvogel and Poulikakos [15] to study thermal spraying of molten ceramic particles.

All the numerical studies listed above modeled essentially the same phenomenon: the normal impact of a droplet onto a flat, solid surface, which can be simulated using a two-dimensional model by assuming that fluid flow is axisymmetric. Though a two-dimensional model is much easier to develop than a fully three-dimensional one, its application is quite limited in modeling spray deposition. For example, in practical applications most droplets do not impact with a velocity normal to the substrate. Indeed there is much interest in modeling impact on steeply inclined planes, which are frequently encountered when applying thermal spray coatings on parts containing cavities, and are the most difficult surfaces to coat. Also, when simulating coating buildup by sequential impact of droplets, a fully three-dimensional model is necessary to model droplet interactions, splashing and breakup.

Bussmann et al. [1] published a description of a three-dimensional, finite-difference, fixed-grid Eulerian model they developed, which used a volume-tracking algorithm to locate the droplet free surface. They simulated water droplets falling with low velocity (~ 1 m/s), onto either an inclined plane or the edge of a step, and compared model predictions with photographs of impacting droplets. Their paper discussed ways of specifying boundary conditions at the liquid–solid contact line, the effect of which is especially important during droplet recoil following impact when fluid flow is dominated by surface tension forces. In a subsequent paper [16], they

used their model to study the splash of a droplet impacting on a solid surface.

The model of Bussmann et al. [1], though three-dimensional, did not consider heat transfer and phase change during droplet impact. Recently Zheng and Zhang [17] developed an adaptive level set method for moving boundary problems and applied the model to droplet spreading and solidification. However, they did not compare their predictions of droplet shape during impact with any experimental evidence. Realistic simulations, which agree well with experiments, require careful attention to the implementation of boundary conditions, including specifying values of the thermal contact resistance at the droplet–substrate interface, and the liquid–solid contact angle.

In this paper we have extended the three-dimensional model of Bussmann et al. [1] to include heat transfer and solidification, and to accommodate the presence of an irregular moving solidification front within the computational grid. To demonstrate that the model gives realistic predictions we simulated deposition of molten tin droplets onto stainless steel surfaces under conditions for which we had experimental results available: the normal impact of a 2.7 mm droplet at 1 m/s onto a cold stainless steel plate and the oblique impact of a 2.2 mm droplet at 2.35 m/s onto a surface inclined at 45°. In both cases the tin droplet was initially at 240 °C (above the melting point, 232 °C) and the stainless steel substrate at 25 °C. These velocities are much lower, and droplet diameters much larger, than those typically encountered in thermal spray applications. However, it is relatively easy to take high quality photographs of impacting droplets under these conditions, and use them to validate predictions from computations. The model, though, is quite general and can be used to examine a wide range of droplet impact conditions. In another study we have used it to simulate thermal spray coating processes [18]. At low impact velocities the effect of surface tension on droplet impact dynamics becomes very important [9]; we have discussed methods of specifying contact angles at moving liquid–solid contact lines and thermal contact resistance at the droplet–substrate interface to obtain realistic simulations.

2. Numerical method

2.1. Fluid flow

Bussmann et al. [1] have given a detailed discussion of the fluid flow model, and it will be reviewed only very briefly here. Fluid flow in an impacting droplet was modeled using a finite-difference solution of the Navier–Stokes equations in a three-dimensional Cartesian coordinate system. The liquid was assumed to be incompressible and any effect of the ambient air on droplet impact dynamics neglected. The fluid flow was taken to be laminar since the flow Reynolds number (assuming radial flow over a flat plate in the droplet after impact) was estimated to be at most 10^4, too small to induce turbulence. The free surface of the deforming droplet was defined using the "fractional volume of fluid" scheme [10]. In this method, a scalar function f is defined as the fraction of a cell volume occupied by fluid. f is assumed to be unity when a cell is fully occupied by the fluid and zero for an empty cell. Cells with values of $0 < f < 1$ contain a free surface. Surface tension was modeled as a volumetric force acting on fluid near the free surface; the method used was the continuum surface force (CSF) model integrated with smoothed values of function f in evaluating free surface curvature. Tangential stresses at the free surface were neglected. Contact angles were applied as a boundary condition at the contact line. For impact on an inclined plane, a simple model described by Bussmann et al. [1] was used to evaluate contact angle as a function of contact line velocity, which required only two input values: the contact angles at the advancing and receding contact lines. Liquid density and surface tension were assumed constant. Liquid viscosity and substrate thermal properties, however, were assumed to vary with temperature. Properties of droplet and substrate materials (tin and stainless steel) were taken from Incropera and DeWitt [19], and Boyer and Gall [20].

2.2. Heat transfer

Heat transfer in the droplet was modeled by solving the energy equation, neglecting viscous dissipation. This assumption can be justified by considering the magnitude of the Eckert number, $Ec = V_o^2/(C_l\Delta T)$, where C_l is the liquid specific heat and ΔT is the temperature difference between the droplet and substrate. For the cases considered here $Ec \sim 10^{-3}$, indicating that the viscous dissipation effects are in fact negligible. Densities of liquid and solid were assumed constant and equal to each other; the values for tin differ by less than 4%, which would have little influence on droplet flow. Using these assumptions, we have

$$\rho\frac{\partial h}{\partial t} + \rho(\vec{V}\cdot\vec{\nabla})h = \vec{\nabla}\cdot(k\vec{\nabla}T). \tag{1}$$

Treatment of the latent heat is a major issue in heat transfer problems involving phase change. Two main numerical techniques have been used to solve such problems: strong solutions and weak solutions [21]. In strong numerical solutions the liquid and solid regions are considered separately; the shape of the phase front is determined by an iterative scheme; and the latent heat of fusion is treated as a heat source at the liquid–solid interface. Strong solutions are not easily extendable to

multidimensional problems. In weak solutions it is not necessary to consider the liquid and solid regions separately: the two phases and the shape of the front between them can be determined later from the solutions. Methods which utilize weak solutions can easily be extended to solve multidimensional problems. Some of these methods commonly used for solidification problems are the *apparent capacity*, *heat integration*, and *enthalpy* methods. Weak methods, by definition, do not specifically account for the discontinuities in a problem and, therefore, cannot be expected to be accurate in the region near the discontinuity. A discontinuity occurs at the phase front in solidification or melting problems. The more severe the discontinuity is, the poorer the performance of the weak methods will be. For water, for example, the ratio of latent heat to sensible heat is about an order of magnitude greater than that for metals. This means that the discontinuity at the phase front for water is much more severe. Therefore, while using weak solutions for water freezing results in poor performance their use for solidification in metals (like tin in this study) is justified.

Since the energy equation has two dependent variables – temperature T and enthalpy h – we used the enthalpy transforming model of Cao et al. [21] to convert the energy equation to one with only one dependent variable: the enthalpy. The main advantage of this method is that it solves the energy equation for both phases simultaneously. The final form, given by Pasandideh-Fard [22], is

$$\rho\frac{\partial h}{\partial t}+\rho(\vec{V}\cdot\vec{\nabla})h=\nabla^2(\beta h)+\nabla^2\phi, \tag{2}$$

where in the solid phase

$$h\leqslant 0;\quad \beta=\frac{k_s}{C_s},\ \ \phi=0, \tag{3a}$$

at the liquid–solid interface

$$0<h<H_f;\quad \beta=0,\ \ \phi=0, \tag{3b}$$

and in the liquid phase

$$h\geqslant H_f;\quad \beta=\frac{k_l}{C_l},\ \ \phi=-\frac{H_f k_l}{C_l}, \tag{3c}$$

where ϕ is a new source term. The energy equation now has only one dependent variable, the enthalpy h. Eqs. (2) and (3a)–(3c) were derived assuming that phase change occurs at a single temperature, as is the case for pure substances. If phase change occurs over a range of temperatures (as happens with alloys), Eqs. (2) and (3a)–(3c) will still be valid, though functions β and ϕ will have different forms [21]. The relationship between temperature and enthalpy is given by

$$T=T_m+\frac{1}{k}(\beta h+\phi), \tag{4}$$

where T_m is the melting point of the droplet. Heat transfer within the substrate is by conduction alone. The governing equation is

$$\rho_w C_w\frac{\partial T_w}{\partial t}=\vec{\nabla}\cdot(k_w\vec{\nabla}T_w). \tag{5}$$

At the free surface of the droplet we used an adiabatic boundary condition. This condition has to be supplemented with the specification of enthalpy h and functions β and ϕ immediately outside the surface, where these values are needed in the finite-difference approximations for points located at the free surface. This was done by setting a zero value for the gradients of the enthalpy h and functions β and ϕ across the free surface. If necessary, the adiabatic boundary condition can easily be modified to account for convection or radiation from the surface, but for the cases under consideration heat transfer to the surrounding air was negligible. Calculations showed that the dominant mechanism of heat loss from an impacting droplet was conduction to the substrate, which was three orders of magnitude larger than convection and radiation from the free liquid surface.

Heat transfer in the droplet and substrate regions was related through the heat flux (q) at the droplet–substrate interface. For the portions of the substrate not covered by the droplet we assumed that there was no heat transfer so that $q=0$. Where the droplet and substrate are in contact, however,

$$q=\frac{(T-T_w)_{\text{substrate}}}{R_c}, \tag{6}$$

where R_c is the thermal contact resistance between droplet and substrate per unit area. Values of R_c were provided as an input to the model. Although in principle R_c could vary with both time and position, we used a constant value in the simulations.

2.3. Solidification

In the presence of a solid phase, computations of the velocity field have to account for the presence of a moving, irregularly shaped solidification front on which the relevant boundary conditions have to be applied. We treated the solidified region of the domain using a modified version of the fixed velocity method. In this approach, a special case of two-phase flow is employed, in which the first phase is the liquid, with volume fraction Θ, and the second phase is the solid, with volume fraction $(1-\Theta)$. The solid is treated as a liquid of infinite density and zero velocity. The volume fraction Θ is a scalar field whose value is equal to one in the liquid and zero in the solid. The definition of Θ differs from that of the function f in that for a liquid flow over its own solid, f is the fraction of a cell

volume occupied by liquid and solid, while Θ is the fraction of a cell volume occupied by liquid and gas. In our model we did not solve for the gas phase, therefore, the void volume replaced the gas volume of a cell. For a cell (i,j,k) of volume $v_{i,j,k}$ the volume fraction Θ is defined as

$$\Theta_{i,j,k} = \frac{1}{v_{i,j,k}} \int \Theta \, \mathrm{d}v. \tag{7}$$

With this definition, Θ is a perfect step function only when solid boundaries coincide with lines of the computational mesh. In general, however, solid boundaries arbitrarily snake through the mesh, cutting through cells. This gives rise to Θ values in the range $0 \leqslant \Theta \leqslant 1$, which is necessary to avoid a 'stair-step' model of a curved interior solid boundary illustrated in Fig. 1 for a 2D coordinate system. As shown in the figure, cells with a value of Θ satisfying $0 < \Theta < 1$ are termed "partial flow cells" because a portion Θ of their finite-difference volume is open to flow and the remaining portion $(1-\Theta)$ is occupied by solid region closed to flow. For partial flow cells, the continuity, momentum and VOF equations are modified as [22]

$$\vec{\nabla} \cdot (\Theta \vec{V}) = 0, \tag{8}$$

$$\frac{\partial(\Theta \vec{V})}{\partial t} + (\Theta \vec{V} \cdot \vec{\nabla}) \vec{V} = \frac{-\Theta}{\rho} \vec{\nabla} p + \Theta \upsilon \nabla^2 \vec{V} + \frac{\Theta}{\rho} \vec{F}_{\mathrm{b}}, \tag{9}$$

$$\frac{\partial f}{\partial t} + (\Theta \vec{V} \cdot \vec{\nabla}) f = 0, \tag{10}$$

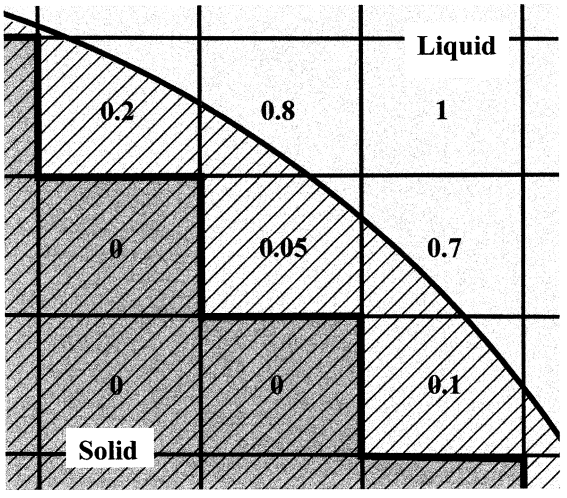

Fig. 1. Representations of the solidification front (hatched area) in two dimensions: a 'stair-step' approximation model; using definition of volume fraction Θ (the corresponding values of Θ are shown).

where $\vec{V}$ represents the velocity vector, p the pressure, ρ the density, υ the kinematic viscosity and $\vec{F}_{\mathrm{b}}$ any body forces acting on the fluid.

Eqs. (8) and (9) were discretized using typical finite-difference conventions on a rectilinear grid covering the volume occupied initially by the droplet plus sufficient volume to accommodate any subsequent free surface deformation. Velocities and pressures are specified on a staggered grid in the traditional fashion: velocities at cell face centres and pressures at the cell centres. Because of the staggered grid we must have a volume fraction Θ at the cell centre, and area fractions Θ_x, Θ_y and Θ_z at the cell faces in the x, y and z directions, respectively. These area fractions can be either calculated from the shape of the solidification front at each time step or approximated based on an average value of the volume fraction Θ in two adjacent cells; results from numerical simulation using the two methods showed no significant differences. The latter method, which was easier to implement, was therefore used.

Eqs. (8) and (9) were solved using a two-step projection method explained in detail by Bussmann et al. [1]. The volume-tracking algorithm used to solve Eq. (10) is the Youngs algorithm [23] that consists of two steps: an approximate reconstruction of the interface followed by a geometric evaluation of volume fluxes across cell faces. The algorithm was shown [1] to produce negligible errors in mass conservation during droplet movement. In our solidification model, explained above, the solid is treated as the liquid with zero velocity. As a result, the solidification model does not affect the accuracy of the volume-tracking algorithm. The free surface was reconstructed by locating a plane within each free surface cell such that the exact value of f is conserved and the unit normal to this plane, $\hat{n}_{\mathrm{l}}$, is directed into the liquid. To evaluate $\hat{n}_{\mathrm{l}}$ we used the following equation in conjunction with a smoothing scheme for function f [1]:

$$\hat{n}_{\mathrm{l}} = \frac{\vec{\nabla} f}{|\vec{\nabla} f|}. \tag{11}$$

Bussmann et al. [1] have given a detailed discretization of Eq. (11). It should be noted that the Youngs algorithm and the evaluation of the unit normal to the liquid using Eq. (11) can only be applied to cells containing no solid. When using the modified fluid flow equations (Eqs. (8)–(10)) our underlying approximation was that for cells partially occupied by solid the computational algorithms used were the same as those used for cells with no solid (Fig. 1). This is because for these cells, the solidified region was characterized as liquid with zero velocity. The fluxes across the cell faces were then corrected based on the value of Θ at the cell faces (Θ_x, Θ_y and Θ_z).

2.4. Boundary conditions at the solid front

Boundary conditions that must be imposed on the surface of the solidified region (solidification front) are velocity boundary conditions and contact angle conditions at the contact line (the line at which the solid, liquid and gas phases meet). Discretization of boundary conditions was done as follows. No-slip conditions were applied by defining "fictitious" velocities within solid cells adjacent to liquid cells. These conditions were only set for solid cells with a zero value of Θ, i.e., on a stair-step representation of the solid surface boundary (Fig. 1). Velocities at the faces of these solid cells were set such that normal and tangential velocities at the liquid-obstacle interface become zero (no-slip condition). It should be mentioned that in our model we treat the solidification front as a sharp interface between the liquid phase and the solid phase. Applying a no-slip boundary condition on this interface is, therefore, reasonable.

Contact angles must be properly set at all points along liquid–solid contact lines. Since these lines were moving we first needed to locate their position in the model. At each time step of calculation, we first identified all vertices of the solid cells adjacent to the contact line: in two dimensions these vertices are all corners of partial flow cells in Fig. 1. A $2 \times 2 \times 2$ computational molecule for each of these vertices was then used to look for a free surface cell (a cell with a value of $\Theta > 0$ that was partially filled with liquid). It should be noted that full cells ($f = 1$) partially occupied by the solid were not considered free surface cells. Finally a $4 \times 4 \times 4$ computational molecule was used to look for an empty cell (a cell with a value of $\Theta > 0$ that was empty of liquid). Any vertex that satisfied the above three conditions was marked as a point on the contact line on which the contact angle was applied. The contact angle was defined here as the angle between the unit normal vector $\hat{n}_l$ directed into the liquid phase and the unit normal $\hat{n}_s$ directed into the solid phase at every point of the contact line as shown schematically in Fig. 2. Evaluation of $\hat{n}_s$ was done in a manner similar to the evaluation of $\hat{n}_l$ (Eq. (11)) as

$$\hat{n}_s = \frac{\vec{\nabla}(1-\Theta)}{|\vec{\nabla}(1-\Theta)|} = -\frac{\vec{\nabla}\Theta}{|\vec{\nabla}\Theta|}. \tag{12}$$

The unit normals $\hat{n}_l$ and $\hat{n}_s$ were evaluated at any vertex of the solid cells adjacent to the contact line (all corners of partial flow cells in Fig. 1). For any vertex marked as a point on the contact line the angle between the two unit normals was obtained from (Fig. 2)

$$\cos(\alpha) = \hat{n}_l \cdot \hat{n}_s. \tag{13}$$

Since the liquid–solid interface was moving, the direction of unit normals $\hat{n}_l$ and $\hat{n}_s$ varied with location on the contact line. As a result, the angle α varied at every point on the contact line at each time step. Proper setting of contact angles at the contact line required that the unit normal $\hat{n}_l$ at every point of the contact line be redirected such that the angle between $\hat{n}_l$ and $\hat{n}_s$ was set to the liquid–solid contact angle θ_{ls} instead of the angle α as shown schematically in Fig. 3. If $\hat{n}_r$ is the redirected unit normal into the liquid phase we will have (Fig. 3)

$$\hat{n}_r = \frac{\sin(\theta_{ls})}{\sin(\alpha)}\hat{n}_l + \frac{\sin(\alpha-\theta_{ls})}{\sin(\alpha)}\hat{n}_s. \tag{14}$$

Finally, the evaluation of $\hat{n}_r$ from the above equation required a known value of the liquid–solid contact angle at every point of the contact line.

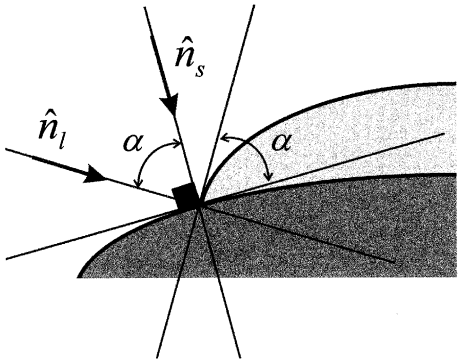

Fig. 2. Schematic of the normal to the liquid free-surface $\hat{n}_l$ and normal to the solidification front $\hat{n}_s$ at one point on the contact line.

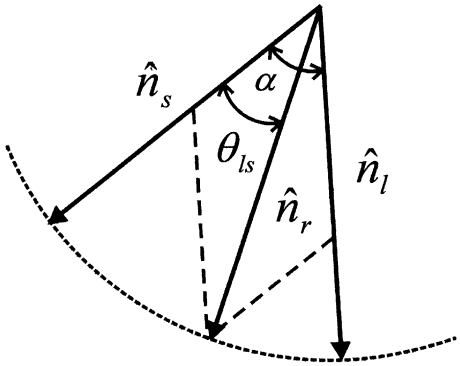

Fig. 3. Schematic of the redirected normal to the liquid free-surface $\hat{n}_r$ based on the liquid–solid contact angle θ_{ls} at one point on the contact line.

2.5. Numerical procedure

The modified Navier–Stokes equations were solved on an Eulerian, rectangular, staggered mesh in a three-dimensional Cartesian coordinate system. The compu-

tational procedure for advancing the solution through one time step was as follows:

1. From time level n values, the velocity and pressure fields as well as f were calculated at time level $n+1$ in accordance with the three-dimensional model of Bussmann et al. [1].
2. Given the droplet enthalpy and substrate temperature fields at time level n, Eqs. (2) and (5) were solved implicitly to obtain the new enthalpy field in the droplet and the new temperature field in the substrate. Temperatures in the droplet were calculated from Eq. (4).
3. New values of the liquid volume fraction Θ were calculated from the enthalpy field in the droplet by using Eqs. (3a)–(3c) in conjunction with an algorithm described by Voller and Cross [24]. In this algorithm, while a change of phase is occurring in the sub-region of a computational cell, the rate of change in the cell enthalpy equals the velocity of the phase change front across the sub-region multiplied by the latent heat of fusion.
4. Flow and thermal boundary conditions were imposed on the free surface, at the solidification front, and the boundaries of the computational domain. In particular, the contact angles were applied at the solidification front (Eq. (14)) and droplet–substrate interface, and the thermal contact resistance at the droplet–substrate interface was applied by using Eq. (6) to calculate the heat flux from the droplet. This value of q was then used to update temperature boundary conditions along the bottom surface of the droplet and the upper plane of the substrate.

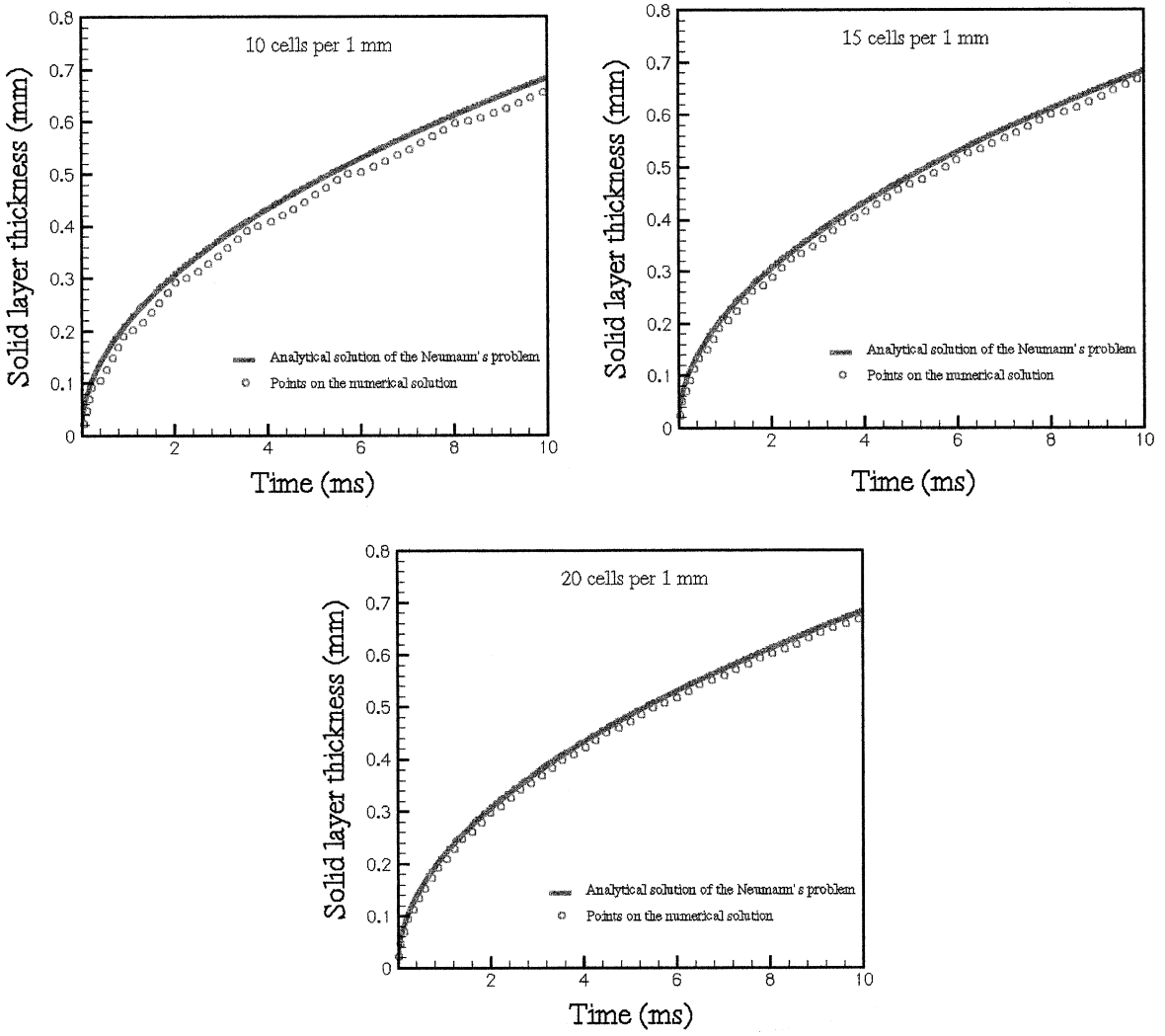

Fig. 4. A comparison between numerical results and analytical solution for the Neumann problem of one-dimensional solidification.

Repetition of these steps allowed advancing the solution through an arbitrary time interval. The droplet was discretized using a computational mesh, with a uniform grid spacing equal to 1/40 of the droplet diameter. The substrate mesh had the same resolution and was extended far enough that its boundaries could be assumed to be at constant temperature. The mesh size was determined on the basis of a mesh refinement study in which the grid spacing was progressively decreased until further reductions made no significant change in

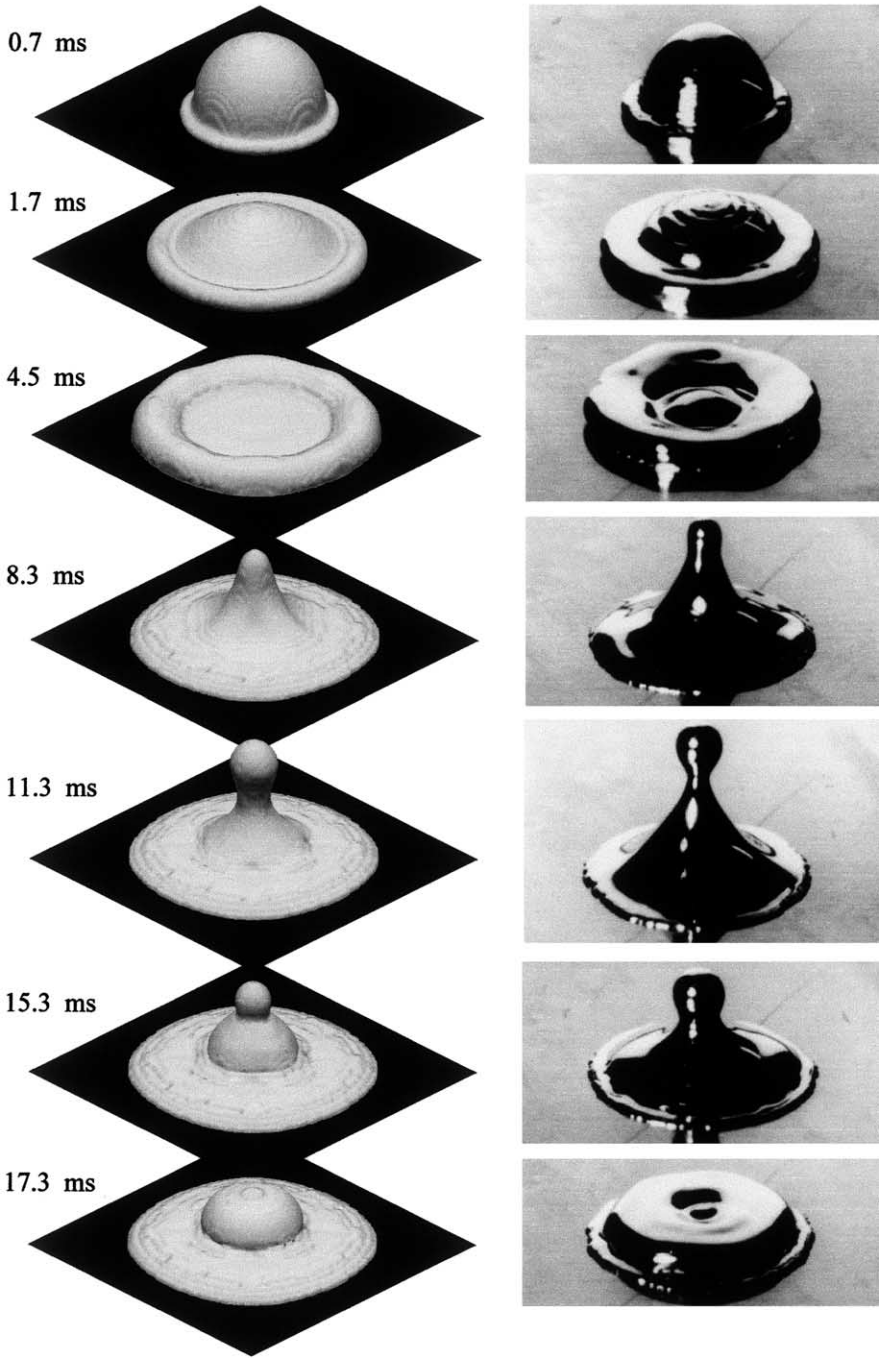

Fig. 5. Computer generated images and photographs of a 2.7 mm diameter tin droplet at 240 °C impacting with a velocity of 1 m/s onto a stainless steel plate initially at 25 °C. Times measured from the moment of impact.

the predicted droplet shape during impact. Bussmann et al. [1] have previously given a detailed description of such a mesh refinement study. Certain restrictions must also be observed in defining the time resolution. Once a mesh is chosen, the choice of the time interval necessary for numerical stability is governed by several restrictions regarding the Courant number (velocity × time interval/ cell size), viscosity, surface tension, and the droplet material liquid and solid thermal diffusivities [22]. For the cases considered in this study, the time intervals were in the order of microseconds. To reduce the computational time, we exploited the planar symmetries of the respective geometries where possible. Numerical computations were performed on a Sun Ultra Enterprise 450 workstation. Typical CPU times for the impact of a droplet on an incline ranged from three to five days.

3. Results and discussion

Before applying the model to droplet impact simulations, we tested its ability to solve a simple problem for which an analytical solution was available. The test case was the Neumann problem of one-dimensional solidification [25], where a molten material is suddenly brought into contact with an isothermal wall whose temperature is below the solidification point of the melt. In our simulation a semi-infinite expanse of molten tin initially at 240 °C contacted a wall at a constant temperature of 25 °C with no contact resistance between the tin and wall. The rate of growth of the solidified layer was calculated from an analytical solution [25] and compared with computational results in Fig. 4. We ran simulations for this problem with a wide range of grid spacing to study the effect of mesh refinement on the solution. Fig. 4 illustrates the results of simulation for three mesh sizes: 10, 15 and 20 cells per 1 mm of tin film thickness. As seen from the figure, numerical results agreed well with analytical solution even for 10 cells per 1 mm thickness of the tin film. Based on these results, and similar mesh refinement studies done during droplet impact simulations, we selected mesh resolutions of between 15 and 20 computational cells per millimeter for the impact simulations shown in this paper.

Fig. 5 shows computer generated images and photographs of the 1 m/s impact of a 2.7 mm diameter tin droplet, with an initial temperature of approximately 240 °C, which is above the melting point of tin ($T_m = 232$ °C). The flow Reynolds number ($V_o D_o/\upsilon$) for this case is 9800. The photographs are taken from a study conducted by Aziz [26,27], who has described the experimental procedure in detail. Tin droplets were deposited with an impact velocity of 1 m/s on a stainless steel surface initially at 25 °C. The time of each image (t), measured from the instant of first contact with the surface, is indicated. Droplets were photographed with a camera pointing downwards at the test surface, inclined at an angle of 30° from the horizontal.

Fig. 6 displays calculated temperature distribution inside the droplet, at the same times following impact as those in Fig. 5. The growth of the solid layer, corresponding to portions of the droplet with $T \leqslant 232$ °C, can be clearly seen in these cross-sectional views.

Photographs and simulations both show that the tin droplet spread on the stainless steel surface following impact, flattened out into a disk with a raised rim, and reached its maximum spread at $t = 4.5$ ms. By this time a solidified layer had formed at the droplet–substrate interface (see Fig. 6). However, there remained a film of molten tin above the solid layer, which surface tension forces prevented from spreading further, so that it recoiled and flowed backwards. The droplet periphery had solidified by this time so that the splat diameter did not change further. Where the recoiling ring of liquid met in the center of the splat a small void was formed (see Fig. 6, $t = 8.3$ ms) that remained in the solidified droplet. The liquid recoiled above the surface ($t = 8.3$–11.3 ms) reaching a maximum height above the surface at approximately 10 ms. Capillary instabilities produced necking in the liquid column (see $t = 11.3$ ms), which was reproduced quite well by the model. Gravity and surface tension pulled back the liquid until it subsided on the solid layer and formed a splat with a rounded upper surface ($t = 17.3$ ms).

Fig. 5 shows good qualitative agreement between photographs and simulations. To compare the two results quantitatively, however, we need to compare the rate of droplet spreading from simulations and experiments. The rate of droplet spreading was quantified by measuring the splat diameter (D) at successive stages during droplet deformation. Normalizing D by the initial droplet diameter (D_o) yields the so-called spread factor ($\xi = D/D_o$). Measured [26] and predicted values of spread factor during the impact are shown in Fig. 7. Agreement with experiments is relatively good, though not exact. The final spread factor from the model differs from that of the experiments by only 6%.

Predictions from the computer model of droplet impact are sensitive to the values of two input parameters: the liquid–solid contact angle (θ_{ls}), and the thermal contact resistance at the droplet–substrate interface. We estimated both of these from experimental measurements. A constant value of $\theta_{ls} = 140$ °C, measured from photographs [26], was specified at the contact line between liquid tin and stainless steel surface during droplet spreading. However, during the recoil (for $t > 4.5$ ms) liquid tin was no longer in contact with stainless steel but flowing on a layer of its own solid (see Figs. 5 and 6). There was no way of

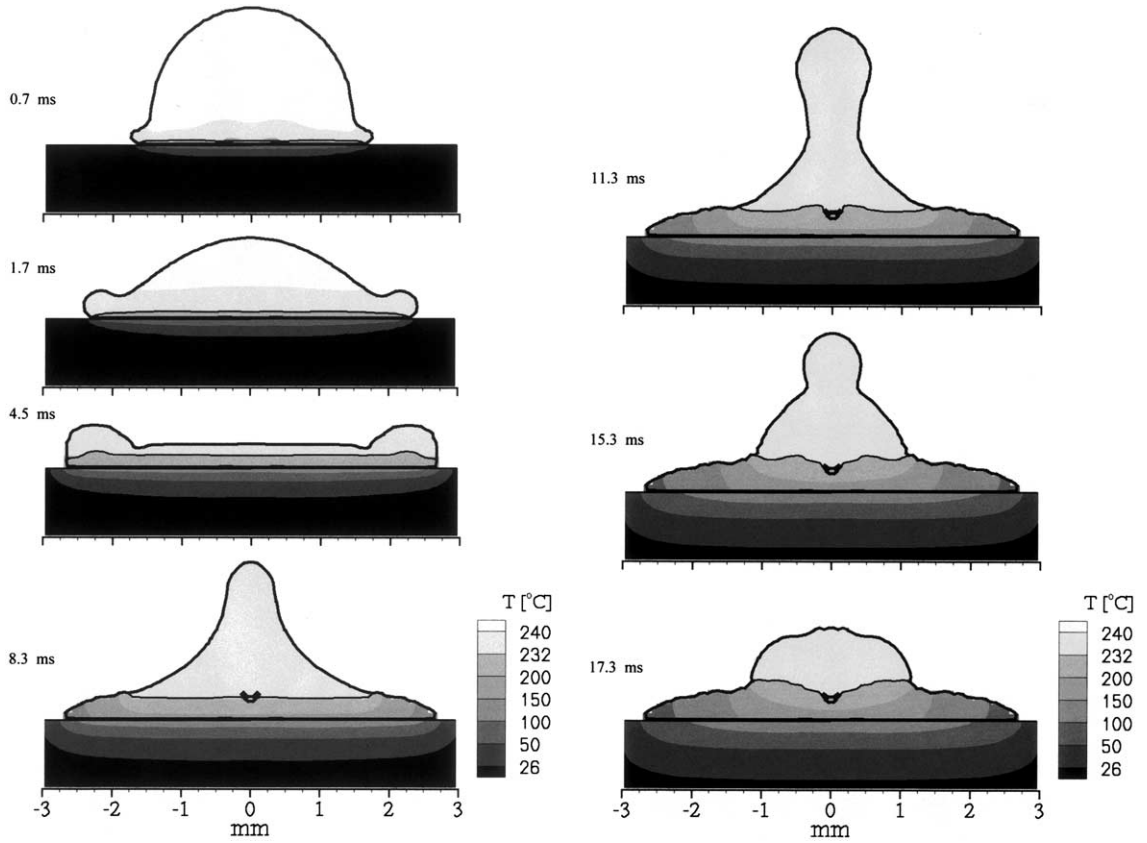

Fig. 6. Calculated temperature distribution inside a 2.7 mm diameter tin droplet initially at 240 °C impacting with a velocity of 1 m/s onto a stainless steel plate initially at 25 °C. Times measured from the moment of impact.

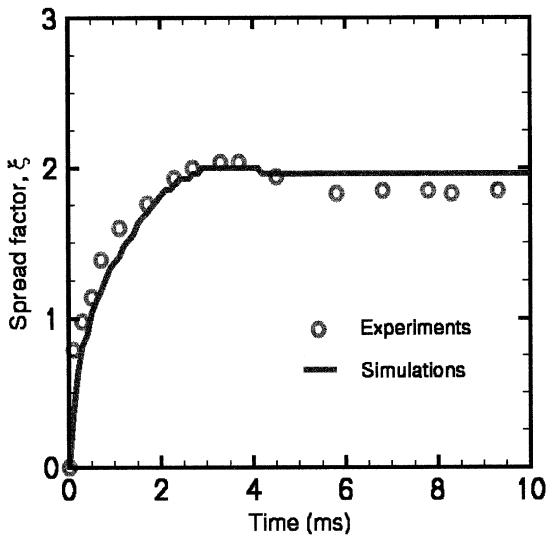

Fig. 7. Evolution of spread factor for the impact of a 2.7 mm diameter tin droplet initially at 240 °C impacting with a velocity of 1 m/s onto a stainless steel plate initially at 25 °C.

measuring the liquid–solid contact angle from photographs, since we did not know the shape and location of the underlying solid layer. As we had no independent method of justifying any assumed variation of the contact angle of molten tin on its own solid during the spread and recoil, we used a constant value of 90°, which produced simulation results that agreed reasonably well with photographs.

Our estimate of thermal contact resistance under the drop was based on previous experimental studies [11,26] of tin droplets dropped onto on a stainless steel surface under conditions similar to those considered here, in which the substrate temperature variation was measured during droplet impact. By fitting these temperature measurements to either a numerical [11] or analytical [26] model, the thermal contact resistance was estimated to be approximately 5×10^{-6} m^2 K/W. All calculations in this paper were performed using this constant value of thermal contact resistance between the tin droplets and the stainless steel surface.

The normal impact of a droplet is relatively simple to model, since liquid flow is symmetric around the droplet

axis and the contact angle is the same all around its circumference. When a droplet hits a surface obliquely there is no longer any axis of symmetry, the contact angle varies around the edges of the droplet, and a three-dimensional model is required to simulate fluid flow.

Fig. 8 shows both computer generated images and photographs of a 2.2 mm tin droplet at 240 °C falling with a velocity of 2.35 m/s onto a stainless steel surface inclined at 45° to the horizontal, that was initially at a temperature of 25 °C. The flow Reynolds number for

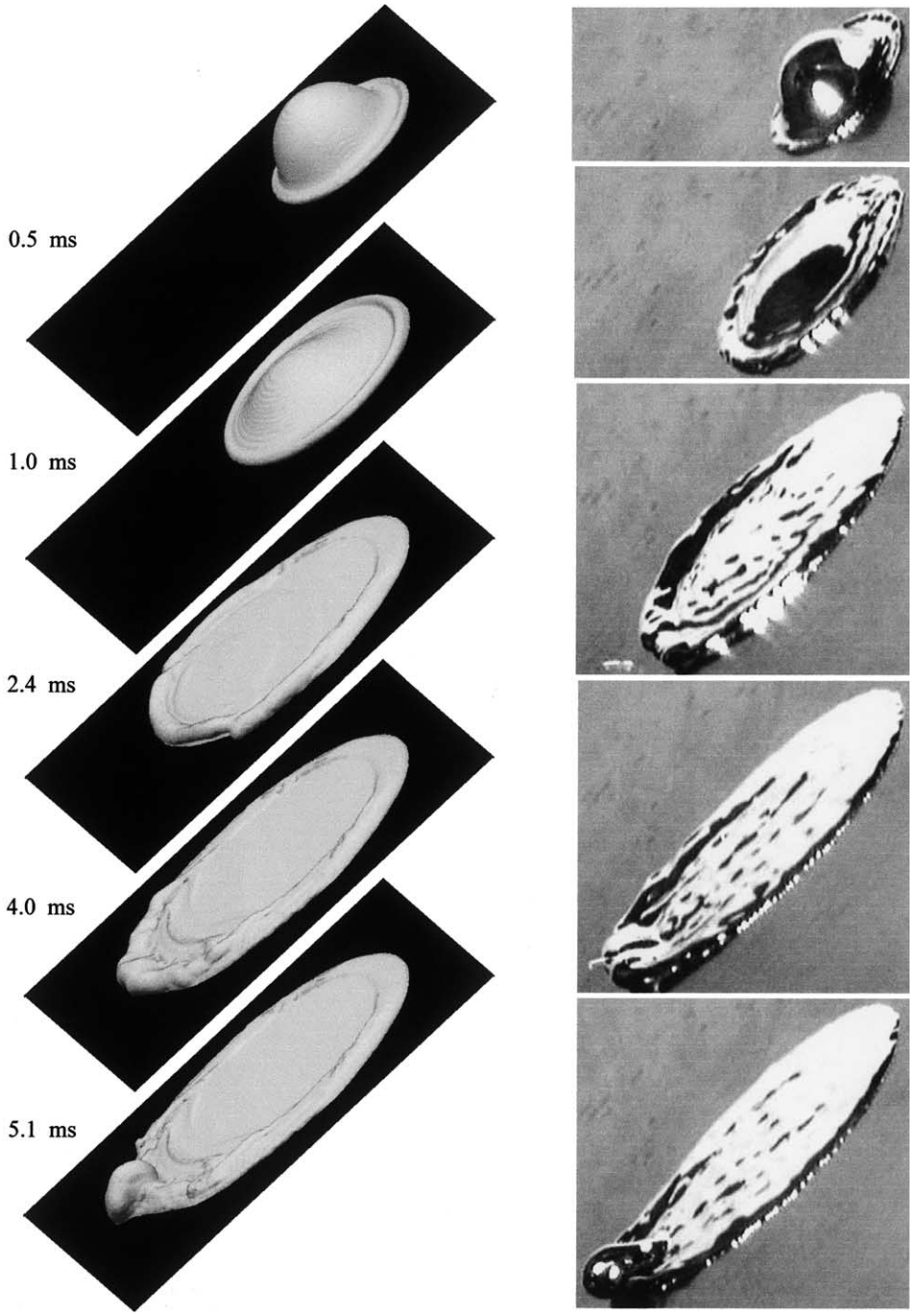

Fig. 8. Computer generated images and photographs of a 2.2 mm diameter tin droplet at 240 °C impacting with a velocity of 2.35 m/s onto a 45° stainless steel incline initially at 25 °C. Times measured from the moment of impact.

this case is 18 800. The elapsed time, measured from the moment of impact, is given to the left of the figures. The photographs were taken from the work of Shakeri [28], where the experiments are described. Fig. 9 shows cross-sectional view of the impacting droplets, with the calculated temperature distribution.

The photographs in Fig. 8 show that the contact angles at the bottom and top of the droplet differ from each other and that the contact angle around the edge of the droplet varies between these two values. To model this variation we used a simple method suggested by Bussmann et al. [1] in which the contact angle depends on whether the contact line is advancing or receding. For liquid tin flowing on a stainless steel surface the advancing angle was assumed to be $\theta_{ls} = 140°$ and for a receding contact line $\theta_{ls} = 40°$, based on measurements from photographs. For the contact angle of liquid tin on its own solid we used the same value applied during the normal impact simulations, 90°.

The behaviour of the droplet (Fig. 8, 0.5 ms) early during impact was similar to that previously observed during normal impact (see Fig. 5), with symmetric spreading of fluid about the point of impact. The symmetry, however, was short-lived and by 1.0 ms the droplet was sliding down the incline. As the droplet moved down it started to freeze and a solid layer appeared at the trailing edge of the droplet as early as 2 ms following impact (Fig. 9). Solidification was fastest at the trailing edge and around the sides of the droplet where the splat was thinnest and the substrate was coldest. The solidification of the edges prevented lateral spreading of the liquid, channeling it downwards (Fig. 8, 2.4 ms). The thickness of the solid layer increased with distance from the top edge (Fig. 9). By $t = 4$ ms most of the kinetic energy of the liquid was lost due to solidification and in overcoming its viscosity, and there was little further movement. The liquid tin flowed over the solidified layer and accumulated near the bottom of the splat as seen in Figs. 8 and 9 at 5.1 ms after the impact. After this time there was no significant fluid flow and the remaining liquid gradually solidified. The final solid splat appeared much as it does in the photograph at $t = 5.1$ ms.

Inspection of Fig. 8, which shows the oblique impact of a tin droplet on a stainless steel surface, demonstrates good qualitative agreement between predictions from the numerical model and experiments. The photographs show a little more liquid at the leading edge of the droplet, perhaps, than was observed in simulations (Fig. 8, $t = 5.1$ ms). It was possible to obtain even better agreement between simulations and experiments by adjusting the value of the thermal contact resistance between the droplet and surface. In reality this value probably changes as the droplet freezes. However, since we had no method of determining how the contact resistance changed, we did not vary it and used the same value of $R_c = 5 \times 10^{-6}$ m^2 K/W in all our calculations.

Measured and predicted spread factor for the oblique impact of tin droplets are displayed in Figs. 10(a) and (b). Fig. 10(a) shows the spread factor measured along the incline (ξ_a, the distance between the leading and trailing edge of the splat normalized by the initial droplet diameter) while Fig. 10(b) shows the spread factor across the incline (ξ_b, the amount of droplet

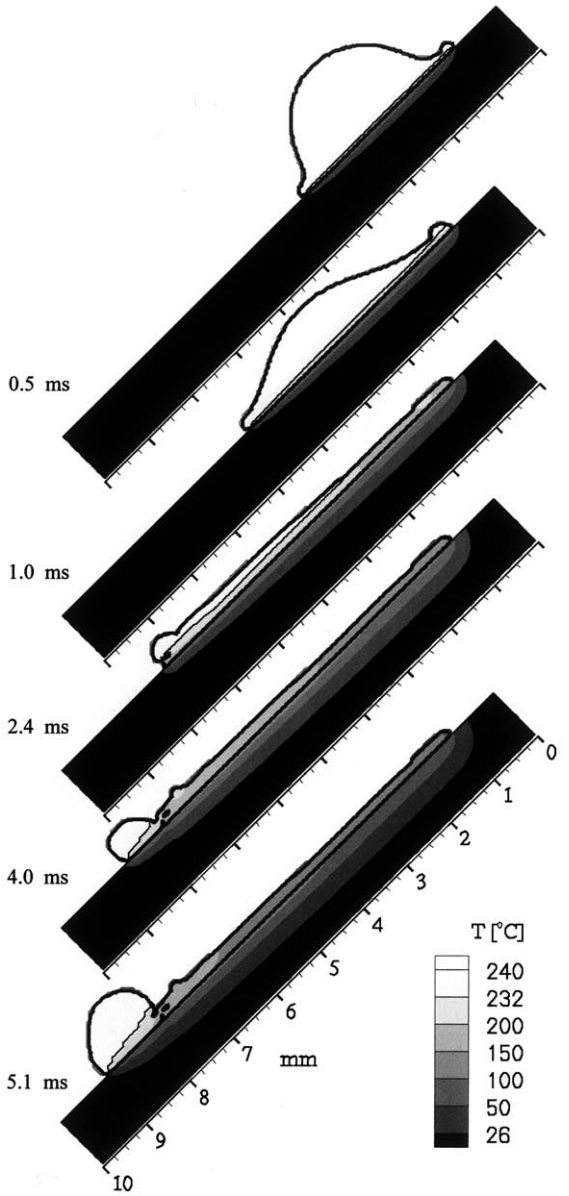

Fig. 9. Calculated temperature distribution inside a 2.2 mm diameter tin droplet initially at 240 °C impacting with a velocity of 2.35 m/s onto a 45° stainless steel incline initially at 25 °C. Times measured from the moment of impact.

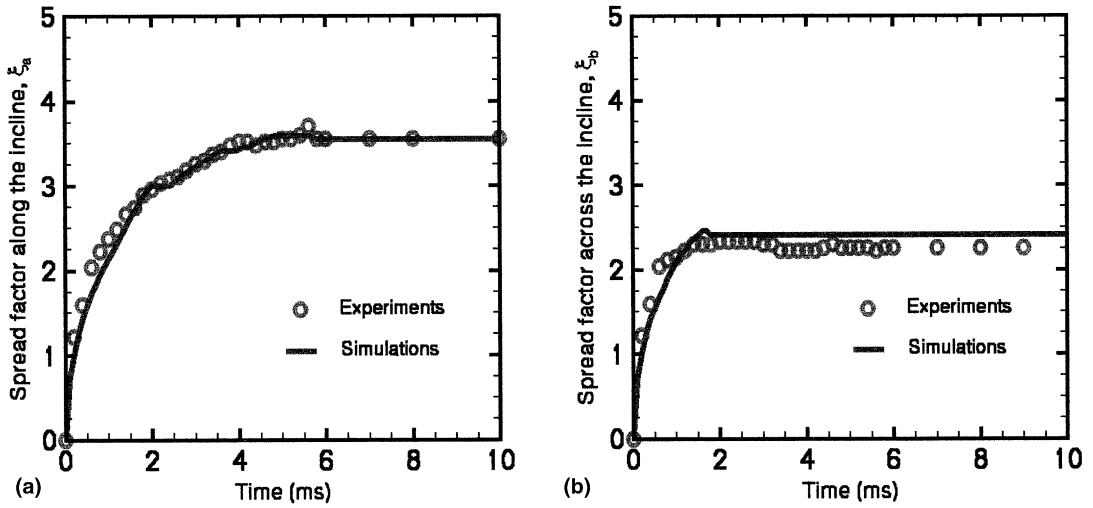

Fig. 10. Evolution of spread factor (a) along the incline (b) across the incline, for a 2.2 mm diameter tin droplet initially at 240 °C impacting with a velocity of 2.35 m/s onto a 45° stainless steel incline initially at 25 °C.

spread to the sides normalized by the initial droplet diameter). Good agreement between predicted and measured values of both spread factors is seen: they differ by less than 5%.

4. Summary and conclusions

We have developed a three-dimensional model of free surface fluid flow with heat transfer and solidification and applied it to simulating the impact of a droplet onto a flat substrate. The model is an extension of one previously developed by Bussmann et al. [1] and combines a fixed-grid control volume discretization of the fluid flow and energy equations with a volume-tracking algorithm to track the droplet free surface and an improved fixed velocity method to track the solidification front. Surface tension is modeled as a volume force acting on fluid near the free surface. Contact angles are applied as a boundary condition at the liquid–substrate and the liquid–solid contact lines. Energy equations in the liquid and solid phases of the droplet are solved using the Enthalpy method. Within the substrate there is only conduction heat transfer. Thermal contact resistance at the droplet–substrate interface is included in the model.

To validate the model we simulated deposition of tin droplets onto both horizontal and inclined stainless steel surfaces. Photographs were presented of such impacts, against which the numerical results were compared; the agreement between the two results was good both qualitatively and quantitatively. Accurate simulation requires specification of liquid–solid contact angles around the edge of the spreading drop and thermal contact resistance under the drop.

Acknowledgements

The authors would like to thank Shiraz D. Aziz and Saeid Shakeri for taking the photographs of tin droplet impact. This research was supported by the Materials and Manufacturing Ontario (MMO), the Natural Sciences and Engineering Research Council of Canada (NSERC), the Canada Foundation for Innovation (CFI), and the member companies of the Thermal Spray Coating Consortium (GE, Sulzer Metco, Hydro Quebec, VAC Aero, Orenda, Pyrogenesis) at the University of Toronto. Their support is gratefully acknowledged.

References

[1] M. Bussmann, J. Mostaghimi, S. Chandra, On a three-dimensional volume tracking model of droplet impact, Phys. Fluids 11 (1999) 1406–1417.
[2] F.H. Harlow, J.P. Shannon, The splash of a liquid droplet, J. Appl. Phys. 38 (1967) 3855.
[3] K. Tsurutani, M. Yao, J. Senda, H. Fujimoto, Numerical analysis of the deformation process of a droplet impinging upon a wall, JSME Int. Ser. II 33 (1990) 555.
[4] G. Trapaga, J. Szekely, Mathematical modeling of the isothermal impingement of liquid droplets in spraying processes, Metall. Trans. B 22 (1991) 901.
[5] FLOW-3D: computational modelling power for scientists and engineers, Technical Report FSI-88-00-1, Flow Science Inc., San Diego, CA, 1988.
[6] H. Liu, E.J. Lavernia, R. Rangel, Numerical simulation of substrate impact and freezing of droplets in plasma spray processes, J. Phys. D 26 (1993) 1900–1908.
[7] D.B. Kothe, R.C. Mjolsness, M.D. Torrey, RIPPLE: a computer program for incompressible flows with free

surfaces, Technical Report LA-12007-MS, LANL, Los Alamos, NM, 1991.
[8] J.U. Brackbill, D.B. Kothe, C. Zemach, A continuum method for modelling surface tension, J. Comput. Phys. 100 (1992) 335–354.
[9] M. Pasandideh-Fard, Y.M. Qiao, S. Chandra, J. Mostaghimi, Capillary effects during droplet impact on a solid surface, Phys. Fluids 8 (1996) 650–659.
[10] C.W. Hirt, B.D. Nichols, Volume of Fluid (VOF) methods for the dynamics of free boundaries, J. Comput. Phys. 39 (1981) 201–225.
[11] M. Pasandideh-Fard, R. Bhola, S. Chandra, J. Mostaghimi, Deposition of tin droplets on a steel plate: simulations and experiments, Int. J. Heat Mass Transfer 41 (1998) 2929–2945.
[12] Z. Zhao, D. Poulikakos, J. Fukai, Heat transfer and fluid dynamics during the collision of a liquid droplet on a substrate-I. Modeling, Int. J. Heat Mass Transfer 39 (1996) 2771–2789.
[13] J. Fukai, Y. Shiiba, T. Yamamoto, O. Miyatake, D. Poulikakos, C.M. Megaridis, Z. Zhao, Wetting effects on the spreading of a liquid droplet colliding with a flat surface: experiment and modeling, Phys. Fluids 7 (1995) 236–247.
[14] M. Bertagnolli, M. Marchese, G. Jacucci, I. St Doltsinis, S. Noelting, Thermo-mechanical simulation of the splashing of ceramic droplets on a rigid substrate, J. Comput. Phys. 133 (1997) 205.
[15] J.M. Waldvogel, D. Poulikakos, Solidification phenomena in picoleter size solder droplet deposition on a composite substrate, Int. J. Heat Mass Transfer 40 (1997) 295–309.
[16] M. Bussmann, S. Chandra, J. Mostaghimi, Modeling the splash of a droplet impacting a solid surface, Phys. Fluids 12 (2000) 3121–3132.
[17] L.L. Zheng, H. Zhang, An adaptive level set method for moving-boundary problems: application to droplet spreading and solidification, Numer. Heat Transfer, Part B 37 (2000) 437–454.
[18] M. Pasandideh-Fard, V. Pershin, S. Chandra, J. Mostaghimi, Splat shapes in a thermal spray coating process: simulations and experiments, J. Thermal Spray Technol. (2002) (in press).
[19] F.P. Incropera, D.P. DeWitt, Fundamentals of Heat and Mass Transfer, third ed., John Wiley and Sons, New York, 1990.
[20] H.E. Boyer, T.L. Gall, Metals Handbook, Desk ed., American Society for Metals, Metals Park, OH, 1995.
[21] Y. Cao, A. Faghri, W.S. Chang, A numerical analysis of Stefan problems for generalized multi-dimensional phase-change structures using the enthalpy transforming model, Int. J. Heat Mass Transfer 32 (1989) 1289–1298.
[22] M. Pasandideh-Fard, Droplet impact and solidification in a thermal spray process, PhD Thesis, University of Toronto, 1998.
[23] D.L. Youngs, An interface tracking method for a 3D Eulerian hydrodynamics code, Technical Report 44/92/35, AWRE, 1984.
[24] V. Voller, M. Cross, An explicit numerical method to track a moving phase change front, Int. J. Heat Mass Transfer 26 (1983) 147–150.
[25] H.S. Carslaw, J.C. Jaeger, Conduction of Heat in Solids, Oxford University Press, London, 1959.
[26] S.D. Aziz, S. Chandra, Impact, recoil and splashing of molten metal droplets, Int. J. Heat Mass Transfer 43 (2000) 2841–2857.
[27] S.D. Aziz, Impact velocity and surface temperature effects on the collision of a molten tin droplet on a solid surface, MASc Thesis, University of Toronto, 1998.
[28] S. Shakeri, Effect of substrate properties on molten metal droplet impact, MASc Thesis, University of Toronto, 2001.